NATIONAL INSTITUTE FOR FUSION SCIENCE

Vlasov and Drift Kinetic Simulation Methods
Based on the Symplectic Integrator

T.-H. Watanabe and H. Sugama

Vlasov and drift kinetic simulation methods based on the symplectic integrator

T.-H.Watanabe and H.Sugama

National Institute for Fusion Science / The Graduate University for Advanced Studies, Toki, Gifu, 509-5292, Japan
(Dated: January 28, 2004)

Vlasov and drift kinetic simulation methods based on the symplectic integrators are benchmarked for test problems on the linear and nonlinear Landau dampings and the Kelvin-Helmholtz (K-H) instability. The explicit symplectic integrator for the separable Hamiltonian straightforwardly leads to generalization of the splitting scheme for the Vlasov-Poisson system. The Nth-order version improves the total energy conservation decreasing the error as $\propto \Delta t^N$ where Δt denotes the time step size. An Eulerian drift kinetic simulation scheme derived from the implicit symplectic integrator for the non-separable Hamiltonian exactly satisfies the conservation of the energy and the enstrophy in the K-H instability, and results in successful application to the plasma echo.

Keywords: Vlasov simulation, drift kinetic simulation, symplectic integrator, simulation method

I. INTRODUCTION

Numerical simulations of the Vlasov and/or drift (gyro-) kinetic equations based on advanced computer technologies have provided a considerable amount of information which is useful for comprehension of kinetic plasma behaviors with strong nonlinearity, and have applied to a wide variety of problems in researches on fusion, space, and astrophysical plasmas. In the Vlasov simulation, the kinetic equation for the one-body velocity distribution function is directly handled as a partial differential equation in the multidimensional phase space, while dynamics of a finite number of macro-particles are calculated in the particle-in-cell simulations [1]. Since Cheng and Knorr [2] proposed the second-order splitting scheme as an efficient time-integration method for the Vlasov-Possion system, numerous investigations on the interpolation method after the time-splitting have been reported [3–13] as well as their applications to various types of nonlinear kinetic plasma phenomena.

The symplectic integrators with high-order accuracy were discovered in early 1990's [14, 15], and rapidly spreads in fields of the Hamiltonian dynamics. Being independent of the study on splitting methods for non-autonomous Hamiltonian equations [16], our previous work deals with application of the fourth-order symplectic integrator to the Vlasov-Possion system as generalization of the second-order splitting scheme [17]. A similar idea is also discussed for the Vlasov-Maxwell equations [10]. To the author's knowledge, however, no systematic benchmark test of the higher-order splitting scheme for the Vlasov equation has not been published yet.

The collisionless drift (gyro-) kinetic equation can be represented in the same compact formula as the Vlasov equation,

$$\frac{\partial f}{\partial t} = -\{f, H\} , \qquad (1)$$

where f and H are the one-body velocity distribution function and the Hamiltonian of a particle, respectively. The Poisson brackets are denoted by $\{,\}$. The standard splitting scheme, however, can not be straightforwardly applied to the drift kinetic equation, since the drift particle Hamiltonian is non-separable for a conjugate pair of the perpendicular coordinates in contrast to the Vlasov-Poisson case where H can be separated into two integrable parts such as the kinetic and potential energies. Thus, a modified type of the time-splitting method has been tested [18, 19], and applied to the ion temperature gradient (ITG) instability [20]. More recently, the semi-Lagrangian scheme [21] is employed for drift kinetic simulations [22, 23]. A nondissipative time-integration method [24] based on the implicit symplectic integrator [25] is also adopted to the drift kinetic simulation of the ITG instability [17, 26, 27], where the time-reversibility and the entropy balance are thoroughly investigated.

In this paper, we consider the Vlasov and drift kinetic simulation schemes which are based on the explicit and implicit symplectic time-integrators, respectively. Conservation properties of invariants in simulations of the Vlasov-Poisson system are investigated in attention to the phase-space resolution. Results of the Vlasov simulations with different orders of the time-integrators are compared to each other in order to examine their properties of the energy conservation that is not guaranteed in the splitting scheme. Here, a nondissipative drift kinetic simulation scheme [17] is also systematically derived from a mapping of f generated by the implicit symplectic integrator. Then, it is numerically verified that the L^2 norm is exactly conserved (except for round-off errors) by use of the nondissipative simulation method.

This paper is organized as follows. After a brief introduction to the higher-order splitting scheme, numerical results for the linear and nonlinear Landau dampings are described in section II. The numerical scheme for the drift kinetic equation is explained in section III as well as the numerical results for the Kelvin-Helmholtz instability. Application to the plasma echo in a drift kinetic system with a two-dimensional slab geometry is given in section III C. Finally, we summarize the results in section IV.

II. HIGHER-ORDER SPLITTING SCHEME FOR THE VLASOV-POISSON SYSTEM

A. Basic algorithm

In order to numerically solve the Vlasov-Poisson equations, Cheng and Knorr have proposed the splitting scheme which consists of three successive transformations of the velocity distribution function f [2],

$$
\begin{cases}
f^*(x,v) = f^n(x - v\Delta t/2, v) \\
f^{**}(x,v) = f^*(x, v - \Delta t \partial \phi/\partial x) \\
f^{n+1}(x,v) = f^{**}(x - v\Delta t/2, v)
\end{cases}
\tag{2}
$$

where the superscripts, n and $n + 1$, denote time steps. The time-integration scheme in Eq.(2) for the Vlasov equation $\partial f/\partial t = -\{f, H\}$ can be regarded as a mapping of f generated by the leap-frog integrator that is widely used in particle-in-cell simulations [1]. Here, $\{,\}$ means the Poisson brackets. In other words, f is advected in the x- (v-) space by Eq.(2) with the velocity v (the acceleration $\partial\phi/\partial x$) which is independent of x (v). Since the leap-frog method is equivalent to the second-order version of the explicit symplectic integrator for the separable Hamiltonian system [15], it is straightforward to extend the splitting scheme into higher-order ones [17].

The Nth-order symplectic integrator for the canonical equation of the generalized coordinates (q,p) with a separable Hamiltonian $H(q,p) = T(p) + V(q)$ is given as [14, 15]

$$
\begin{cases}
q_i = q_{i-1} + c_i\Delta t(\partial T/\partial p)_{p=p_{i-1}} \\
p_i = p_{i-1} - d_i\Delta t(\partial V/\partial q)_{q=q_i}
\end{cases}
(i = 1, ..., k) ,
\tag{3}
$$

with $(q_0, p_0) = (q^n, p^n)$ and $(q_k, p_k) = (q^{n+1}, p^{n+1})$. For the first-order scheme ($N = 1$), $k = 1$ and $c_1 = d_1 = 1$. The second-order ($N = 2$) method which is equivalent to the leap-frog integrator consists of $k = 2$, $c_1 = c_2 = 1/2$, $d_1 = 1$, and $d_2 = 0$. The fourth-order integrator ($N = 4$ and $k = 4$) has been derived by Forest and Ruth [14] such that

$$
c_1 = c_4 = \frac{1}{2(2 - 2^{1/3})} , \quad c_2 = c_3 = \frac{1 - 2^{1/3}}{2(2 - 2^{1/3})} ,
$$

$$
d_1 = d_3 = \frac{1}{2 - 2^{1/3}} , \quad d_2 = -\frac{2^{1/3}}{2 - 2^{1/3}} , \quad d_4 = 0 \tag{4}
$$

Yoshida has systematically derived the higher-order schemes for even numbers of N which are represented by successive operations of the second-order integrator S_2. For example, the fourth-order integrator denoted by S_4 is represented as [15]

$$
S_4(\Delta t) = S_2(d_1\Delta t)S_2(d_2\Delta t)S_2(d_1\Delta t) ,
\tag{5}
$$

where d_1 and d_2 are defined in Eq.(4). He also numerically obtained the coefficients for the sixth- ($N = 6$ and $k = 8$) and the eighth-order ($N = 8$ and $k = 16$) schemes [15].

The higher-order time-integration scheme for the Vlasov equation is obtained by applying the explicit symplectic integrator to the coordinate transformations in the time-splitting scheme as follows [17];

$$
\begin{cases}
f^*_{i-1}(q,p) = f_{i-1}(q - c_i\Delta t \, \partial T/\partial p|_{f=f_{i-1}}, p) \\
f_i(q,p) = f^*_{i-1}(q, p + d_i\Delta t \, \partial V/\partial q|_{f=f^*_{i-1}})
\end{cases}
(i = 1, ..., k) .
\tag{6}
$$

For an even number of N, Eq.(6) can also be given by successive operations of the second-order splitting scheme, Eq.(2), in accordance to the Nth-order symplectic integrator by Yoshida. A similar formulation for the Vlasov-Maxwell system is also discussed by Mangeney et al. [10]. In the followings, results of the benchmark tests for the generalized splitting scheme in Eq.(6) are shown for $N = 1, 2, 4$, and 6.

B. Benchmark tests for Landau damping

1. Simulation code

Here, we compare the splitting schemes with different orders of integrators. Let us consider the normalized Vlasov-Possion equations,

$$
\frac{\partial f}{\partial t} + v\frac{\partial f}{\partial x} + \frac{\partial \phi}{\partial x}\frac{\partial f}{\partial v} = 0 ,
\tag{7}
$$

$$
-\frac{\partial \phi^2}{\partial x^2} = 1 - \int_{-\infty}^{+\infty} f \, dv ,
\tag{8}
$$

where f denotes the distribution function for electrons. Stationary background ions are assumed. Physical variables in the above equations are normalized by using the electron thermal speed, v_t, the angular plasma frequency, ω_p, and the electron temperature, T_e. The computational domain is defined in $0 \le x < L$ and $-v_{max} \le v \le v_{max}$ with the periodic boundary condition in the x-direction, and is discretized by numerical grid points of $(N_x, 2N_v + 1)$ with equal spacings. Since our concern here is to check accuracy of the time-integration schemes with different orders, it is preferable to separate their numerical errors from those associated with finite phase-space resolution. Thus, it is necessary to keep enough resolution in the phase space.

In the applications given below, the coordinate transformations in calculation of the mapping of f are carried out by means of the Fourier mode interpolation [4, 5] in order to accurately evaluate errors in conservation of the invariants. The transformation of $x - vc_i\Delta t$ is calculated in the Fourier space by multiplying a phase shifting factor of $\exp(-ikvc_i\Delta t)$. Similarly, the transformation of $v - d_i\Delta t\partial\phi/\partial x$ is given by multiplying $\exp(-i\ell d_i\Delta t\partial\phi/\partial x)$ in the velocity wave number (ℓ) space. Because of the finite resolution, the simulation scheme works well only when scale lengths of interest in

the phase space are much greater than the grid spacings ($k \ll \pi/\Delta x$ and $\ell \ll \pi/\Delta v$). Therefore, it is necessary to stop the simulation run before the finest scale length of f in the phase space becomes comparable to the grid size because of the phase mixing.

In order to enable numerical calculation of the entropy $S \equiv -\int f \ln f \, dx dv$, we simply set the minimum value of f to that given in the initial condition in case infinitesimal negative values of f appear on a tail of distribution at large absolute values of the velocity due to round-off errors. Since the value is quite small [$\sim O(10^{-22})$], effects of the above treatment for avoiding negative f values on the main results discussed below are on the order of round-off errors, if the distribution function is well represented by a finite number of grid points with enough resolution. When the resolution becomes insufficient during the simulation run, however, the entropy unphysically changes in a short time, which can be used as an indicator of soundness of the numerical simulation as shown in Fig.3.

The periodic treatment of f in association with the Fourier interpolation in the v-space is justified by setting sufficiently large v_{max}, even though it is different from the rigorous boundary condition that $f \rightarrow 0$ for $v \rightarrow \pm\infty$. Here, we set $v_{max} = 10 v_t$ where the Maxwellian distribution function [$F_M = \exp(-v^2/2v_t^2)/\sqrt{2\pi}v_t$] has a quite small amplitude of $\sim O(10^{-22})$.

2. Linear Landau damping

A benchmark test for the linear Landau damping has been considered in literatures [11, 13], where the initial condition is given by

$$f(x, v, t = 0) = \frac{1}{\sqrt{2\pi}} \exp(-v^2/2)(1 + \alpha \cos kx) \quad (9)$$

with $\alpha = 0.01$ and $k = 0.5$. The system length $L = 4\pi$. For discretization of the simulation domain, we have employed 32×513 grid points ($N_x = 32$ and $N_v = 256$). The recurrence time for the $k = 0.5$ mode is estimated as $\tau_r = 2\pi/k\Delta v = 321.7$ (for $\Delta v = N_v/v_{max}$) which is much longer than the simulation time of $t = 50$ shown in Fig.1. Since the nonlinear mode coupling is very weak for $\alpha = 0.01$, it is enough to take $N_x = 32$. From the linear theory, real and imaginary parts of the eigenfrequency for $k = 0.5$ are evaluated as $\omega_r = 1.4156$ and $\gamma = -0.1533$, respectively.

Time evolutions of the electric field amplitude of the fundamental mode with $k = 0.5$ are shown in Fig.1. The entropy S is well conserved throughout the simulation runs (normalized errors are less than 5×10^{-11}), which are discussed in the next section in more detail in association with conservation properties of the total energy and other invariants. The results from the first-, second-, fourth-, and sixth-order methods for $\Delta t = 1/8$ are plotted in the top panel where no distinct difference is found for different orders. The obtained values of $\omega_r = 1.416$
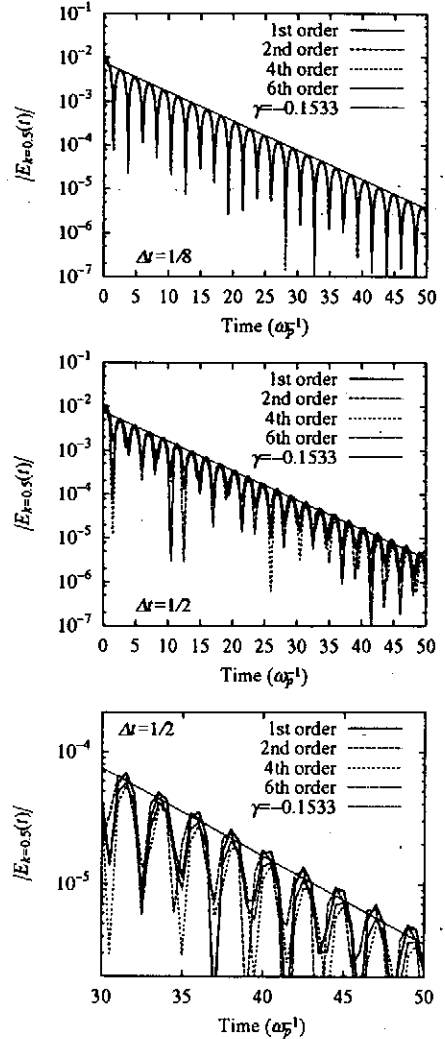

FIG. 1: Time evolutions of electric field amplitude with $k = 0.5$ during the linear Landau damping obtained by first-, second-, fourth-, and sixth-order time-integration methods with $\Delta t = 1/8$ (top) and $1/2$ (middle and bottom). Vertical and horizontal axes in the middle panel are magnified on the bottom for clarity.

and $\gamma = -0.153$ agree well with the linear calculation. As plotted in the middle and bottom panels of Fig.1, however, small differences are found in the damping rates for $\Delta t = 1/2$, which are also summarized in Table I. The error found in the damping rate is about 3% in the first-order method. The better agreement with the theoretical estimate is found for the higher-order schemes.

— 3 —

Order	γ
1	−0.148
2	−0.149
4	−0.154
6	−0.153

TABLE I: Linear Landau damping rates resulted from the simulations with different orders of integrators for $\Delta t = 1/2$.

3. Nonlinear Landau Damping

A benchmark test for the nonlinear Landau damping has also been considered in literatures [2, 6, 8, 9, 12, 13], where the initial condition is given by Eq.(9) with $\alpha = 0.5$. Since more particles are trapped by waves with larger amplitudes, finer-scale structures of f are generated by the phase mixing not only in the v-space but also in the x-space. In other words, the distribution function is strongly stretched by the Hamiltonian flow in the phase space. In order to keep sufficient resolution during the simulation till $t = 40$, thus, we employed grid points of $N_x = 4096$ and $N_v = 65536$ for the results shown in Figs.2, 4, and 5.

Following the exponential damping of the initial perturbation, the nonlinear particle trapping as well as the strong mode coupling is observed in the simulation. A more detailed picture of the benchmark problem is found, for example, in Ref.[13]. Here, we focus on conservation properties of the invariants in simulations with the splitting schemes of different orders. The entropy S, the L^1 and L^2 norms ($L^1 \equiv \int f dx dv$ and $L^2 \equiv \int f^2 dx dv$) are preserved well throughout the simulation run up to $t = 40$ with $\Delta t = 1/8$ as shown in Fig.2. The errors found in the invariants are negligibly small, as typically seen in the stepwise increase of the L^1 norm corresponding to the round-off error level of the double precision numbers. The fourth- and the sixth-order schemes lead to about three and seven times larger errors than that found in the second-order case, respectively. The factors correspond with the number of the successive operations of the second-order integrator constructing the higher-order schemes. Magnitude of the errors is also proportional to the inverse of the time step size Δt^{-1} (not shown), but is insensitive to the number of grid points as shown in Fig.3, if sufficient phase-space resolution holds. In a simulation without setting the minimum value of f, the L^2 norm increases with the nearly same rate as that in the case with setting the minimum f (as shown by the dot-dashed line on the bottom of Fig.2 for the fourth-order case), while the L^1 norm is exactly conserved. It is, therefore, concluded that the errors in the entropy and the L^2 norm shown in Fig.2 are mainly due to accumulation of the round-off errors in numerical time-integrations. We have also confirmed similar behaviors of L^3, L^4, and L^5 norms (not shown). Conservation of the L^1 norm is slightly broken on the order of 10^{-13} by setting the minimum
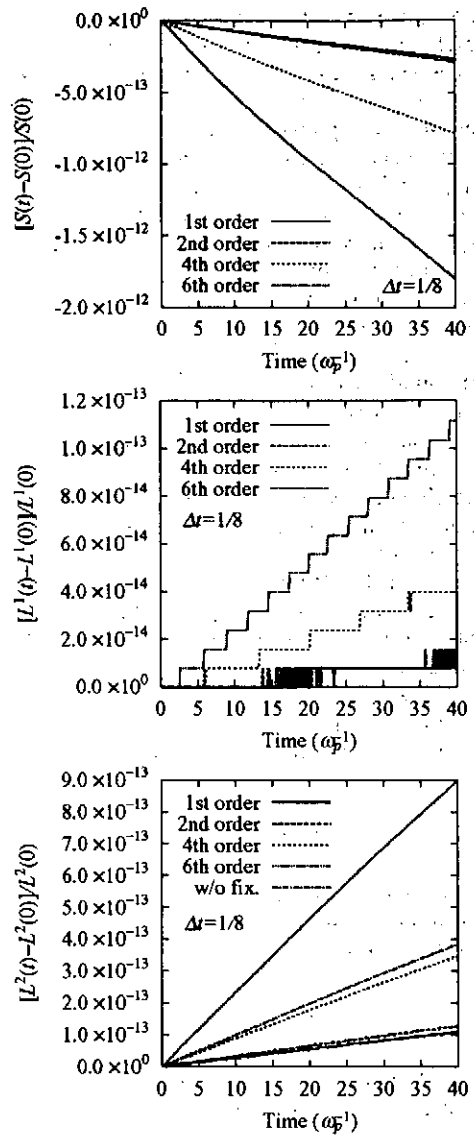

FIG. 2: Time evolutions of errors found in the entropy (top) and the L^1 (middle) and L^2 (bottom) norms during the nonlinear Landau damping obtained by simulations with the first-, second-, fourth-, and the sixth-order time-integration methods for $\Delta t = 1/8$. The dot-dashed curve on the bottom is also given by the fourth-order scheme but in a case without setting the minimum value of f.

amplitude of f that is introduced in order to enable the entropy calculation.

The invariants given by the phase-space integral of the Vlasov equation multiplied by f^m ($m = -1, 0, 1, ...$) are well preserved if a sufficient number of grid points are employed. In the early stage of the simulations, the errors found in the entropy for cases with different resolution show similar evolutions to those given in Fig.2 (see the

FIG. 4: Time evolutions of errors found in the total energy conservation during the nonlinear Landau damping obtained by simulations with the first-, second-, fourth-, and the sixth-order time-integration methods for $\Delta t = 1/8$.
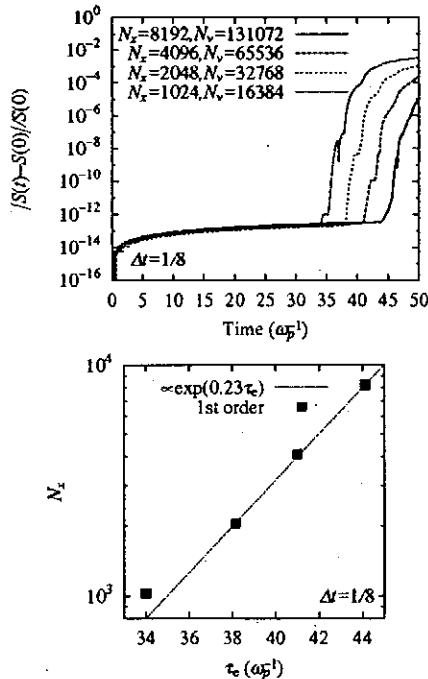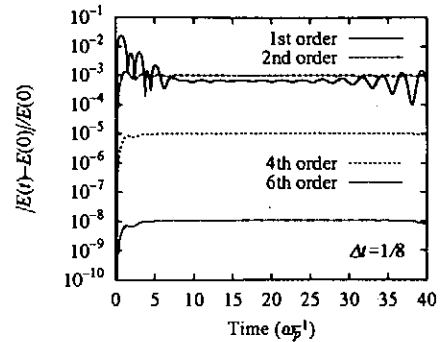

FIG. 3: Time evolutions of errors found in the entropy resulted from simulations with different phase-space resolution (top). Number of grid points in the x-space (N_x) plotted for the eruption time of the entropy τ_e (bottom).
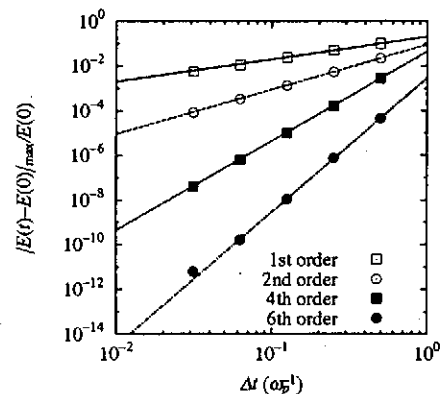

FIG. 5: Summary of the total energy conservation in simulations of the nonlinear Landau damping. Solid, dashed, dotted and dot-dashed lines represent $\propto \Delta t^\beta$ where $\beta = 1, 2, 4$, and 6, respectively.

top panel of Fig.3, where we have employed the first-order scheme with $\Delta t = 1/8$ while keeping the ratio of N_v to N_x constant). After the finest scale length of f reaches the grid size, however, the error rapidly blows up. The eruption time τ_e of the entropy is summarized in the bottom of Fig.3, where one can see that the finer grid size leading to larger τ_e makes the longer simulation possible. However, N_x exponentially increases as τ_e, which means that the smallest scale length of f shortens exponentially in time because of the stretching of f in the phase space. It also occurs simultaneously with the nonlinear particle trapping.

Conservation of the total energy definitely depends on the accuracy of the time-integration scheme. Time evolutions of total energy fluctuations for $\Delta t = 1/8$ are plotted in Fig.4. One can confirm that the energy conservation is certainly improved by applying the higher-order splitting scheme. In addition, there is no secular increase nor decrease of the energy after $t \approx 5$.

Dependence of the error in the energy conservation, which is defined by $|E(t) - E(0)|_{max}/E(0)$, on the time step size is summarized in Fig.5, where the solid, dashed, dotted and dot-dashed lines represent powers of Δt such as $\propto \Delta t^\beta$ with $\beta = 1, 2, 4$, and 6, respectively. The time step size Δt is changed as 1/2, 1/4, 1/8, 1/16, and 1/32. The total energy conservation is improved in proportional to Δt^N where N denotes the order of the time-integration scheme.

III. NONDISSIPATIVE TIME-INTEGRATION METHOD FOR THE DRIFT KINETIC SYSTEM

A. Basic algorithm

The symplectic integrator is also useful for construction of a nondissipative simulation scheme for the collisionless drift kinetic equation which possesses the same compact form of $\partial f/\partial t = -\{f, H\}$ as the Vlasov equation. Even in a slab configuration with the uniform magnetic field, however, the splitting algorithm based on the explicit symplectic integrator, Eq.(6), can not be applied to the drift kinetic system, because the Hamiltonian of an $\boldsymbol{E} \times \boldsymbol{B}$ drift particle, $H = v_\parallel^2/2 + \phi(\boldsymbol{x}_\perp, x_\parallel)$ (normalized), is non-separable for a conjugate pair of the perpendicular

coordinates, $x_\perp = (x_{\perp 1}, x_{\perp 2})$. Here, $x_\parallel$ and $v_\parallel$ are the parallel coordinate and velocity, respectively.

An implicit symplectic integrator is applicable to a general type of Hamiltonian. One of the simplest methods is given by

$$\begin{pmatrix} q^{n+1} \\ p^{n+1} \end{pmatrix} = \begin{pmatrix} q^n \\ p^n \end{pmatrix} + \Delta t \begin{pmatrix} \partial H/\partial p|_{\bar{q},\bar{p}} \\ -\partial H/\partial q|_{\bar{q},\bar{p}} \end{pmatrix}, \quad (10)$$

where $\bar{q} = (q^n + q^{n+1})/2$ and $\bar{p} = (p^n + p^{n+1})/2$. The time-integration scheme in Eq.(10) with the second-order accuracy is called the implicit midpoint rule. For canonical coordinates (q, p), Eq.(10) gives a canonical transformation, and then, is an implicit symplectic integrator [25]. Extension of Eq.(10) to the 4th-order method is straightforward in terms of the same successive operations as Eq.(5).

Using a compact form of the coordinates, $z = (q, p)$, one can rewrite Eq.(10) to

$$z^{n+1} = z^n + \Delta t \{z, H(\bar{z})\} \quad \text{with} \quad \bar{z} = \frac{z^{n+1} + z^n}{2}. \quad (11)$$

For the collisionless kinetic equation, $\partial f/\partial t = -\{f, H\}$, a mapping of f generated by Eq.(11) can be represented as

$$f^{n+1}(z) = f^n [z - \Delta t \{z, H(\bar{z})\}]. \quad (12)$$

If one considers an intermediate time-step, $t^{n+1/2}$, the mapping in Eq.(12) is similar to the transformation used in the semi-Lagrangian method [21, 22]. There is, however, a difference between the two transformations. In Eq.(12), $H(\bar{z})$ implicitly depends on f^{n+1} through ϕ^{n+1}, while the operator (the Hamiltonian flow in this case) employed for calculation of the characteristics in the semi-Lagrangian scheme is obtained from f at the intermediate time step that has been known before evaluating f^{n+1}.

Since direct calculation of the mapping in Eq.(12) is somewhat difficult because of the implicit dependence of $H(\bar{z})$ on f^{n+1}, we would employ a simplified algorithm for the drift kinetic system. A symmetric transformation from f^n to f^{n+1} can also be generated by Eq.(11),

$$f^{n+1}[z + (\Delta t/2)\{z, H(\bar{z})\}] = f^n[z - (\Delta t/2)\{z, H(\bar{z})\}]. \quad (13)$$

We consider the Taylor expansion of f^{n+1} and f^n for a small time step Δt, such that

$$\begin{aligned} f^{n+1}[z + (\Delta t/2)\{z, H(\bar{z})\}] \\ \approx f^{n+1}(z) + (\Delta t/2)\{f^{n+1}, H(\bar{z})\}, \end{aligned} \quad (14)$$

and

$$\begin{aligned} f^n[z - (\Delta t/2)\{z, H(\bar{z})\}] \\ \approx f^n(z) - (\Delta t/2)\{f^{n-1}, H(\bar{z})\}. \end{aligned} \quad (15)$$

Substitution of Eqs.(14) and (15) into Eq.(13) yields

$$f^{n+1} = f^n - \Delta t \{\bar{f}, \bar{H}\} \quad \text{with} \quad \bar{f} = \frac{f^{n+1} + f^n}{2}. \quad (16)$$

The time-integration scheme in Eq.(16) corresponds to the implicit midpoint rule applied to f (not to z), and has the second-order accuracy because of the symmetry for f^{n+1} and f^n. The time-reversibility of the collisionless kinetic equation is also preserved by using Eq.(16). The fourth-order version of this scheme can be easily constructed by successive operations of Eq.(16) in the same way as Eq.(5) [17, 24].

It is important to note that, when the implicit midpoint rule is applied to an advection equation for a vector field U in an incompressible flow V, that is,

$$\frac{\partial U}{\partial t} = -V \cdot \nabla U \quad \text{with} \quad \nabla \cdot V = 0, \quad (17)$$

conservation of $|U|^2$ is guaranteed, such that

$$|U^{n+1}|^2 - |U^n|^2 = -\Delta t \nabla \cdot \left(|\bar{U}|^2 V\right). \quad (18)$$

Since the Hamiltonian flow is incompressible in the phase space, Eq.(16) leads to

$$|f^{n+1}|^2 - |f^n|^2 = -\Delta t \left\{|\bar{f}|^2, \bar{H}\right\}. \quad (19)$$

In a system with the periodic boundary condition for the real space, or, if the surface integrals can be omitted, the L^2 norm ($\int f^2 d^3x dv_\parallel$) is conserved during the numerical time-integration (where $f \to 0$ for $v_\parallel \to \pm\infty$ is assumed). In this sense, the time-integration method in Eq.(16) is nondissipative, which is a great advantage in simulations of the collisionless ITG turbulent transport [17, 26, 27].

B. Benchmark test for Kelvin-Helmholtz instability

1. Test problem and simulation code

As a benchmark test of simulation methods for the drift kinetic system, the Kelvin-Helmholtz (K-H) instability described by the two-dimensional Euler equation has been considered in literatures [18, 22]. The drift kinetic equation in a two-dimensional slab geometry with the translational symmetry in the direction of the homogeneous magnetic field has the same form as the vorticity equation,

$$\frac{\partial \rho}{\partial t} + \frac{\partial \psi}{\partial x}\frac{\partial \rho}{\partial y} - \frac{\partial \psi}{\partial y}\frac{\partial \rho}{\partial x} = 0, \quad (20)$$

where ρ and ψ denote the vorticity and the stream function, respectively, and are related by the Poisson equation,

$$\nabla^2 \psi = -\rho. \quad (21)$$

Here, we obey the notation used in Ref.[18]. In the benchmark test, the equilibrium flow given by $\rho_0(y) = \sin y$ is unstable to a perturbation of $\rho_1(x,y) = \epsilon \sin(y/2)\cos(k_1 x)$ if $k_1 < k_s = \sqrt{3}/2$ [28]. We have performed a test simulation with the same initial condition as that employed in Ref.[22], that is,

$$\rho(x,y,t=0) = \rho_0(y) + \rho_1(x,y) \qquad (22)$$

for $\epsilon = 0.015$ and $k_1 = 2\pi/10$.

The simulation domain of $0 \leq x < 10$ and $0 \leq y \leq 2\pi$ is discretized by a uniform mesh of 512×513. The periodic boundary condition is employed in the x-direction while $\rho = \psi = 0$ at $y = 0$ and 2π. Adding an extra region of $-2\pi \leq y < 0$ with the anti-symmetry condition, $\rho(y) = -\rho(-y)$, enables us to use the pseudo-spectral method in calculation of the advection term where the 2/3-rule is adopted for de-aliasing [29]. The numerical time-integration of Eq.(20) is carried out by using the nondissipative integrator in Eq.(16) with the second-order accuracy where $f = \rho$ and $H = -\psi$. We set the time-step size $\Delta t = 5 \times 10^{-3}$ so as to find convergence of the iteration loop in solving Eq.(16). The iteration is stopped if $|\rho^j - \rho^{j-1}|_{\max}/\overline{\rho^j} \leq 10^{-15}$, where j and $\overline{\cdots}$ mean the iteration step and the root-mean-square average, respectively.

2. Numerical results

Time evolution of the vorticity perturbation with $k_x = k_1$ is shown in Fig.6 in terms of $\langle |\rho(k_x = k_1, y)|^2 \rangle_y$, where $\langle \cdots \rangle_y$ denotes the spatial average in the y-direction. The solid curve in the linear growth phase is fitted by $\propto \exp(0.226t)$. Thus, the linear growth rate of the K-H instability obtained by the simulation is 0.113, which is in reasonable agreement with the theoretical estimate in the first-order approximation, that is, $\mathrm{Im}(\omega) = \sqrt{3}k_1(k_s - k_1)/2 = 0.129$ for $k_s = \sqrt{3}/2$ [28]. Although the evolution of $\langle |\rho(k_x = k_1, y)|^2 \rangle_y$ obtained by a simulation without de-aliasing is nearly identical to that in the de-aliased case (see Fig.6), remarkable differences are found in conservation of the energy $E = \int |\nabla\psi|^2 dx dy$ and the enstrophy $\Omega = \int \rho^2 dx dy$ as shown in Fig.7. Since ψ is related to ρ by Eq.(21), conservation of the energy is also guaranteed by employing the nondissipative time-integration scheme as shown by Eq.(16). In the simulation with the 2/3-rule for de-aliasing, thus, relative errors in the energy and enstrophy conservation are less than 10^{-15} throughout the simulation run up to $t = 50$, which is the benefit in use of the nondissipative integrator. In the case without the de-aliasing technique, however, the energy and enstrophy conservation rapidly degrades after $t \sim 27$ due to the aliasing error. It means that the smallest scale lengths of ρ and ψ become comparable to, and then, shorter than twice of the grid size (the Nyquist wave length) because of the strong nonlinearity of the advection term.
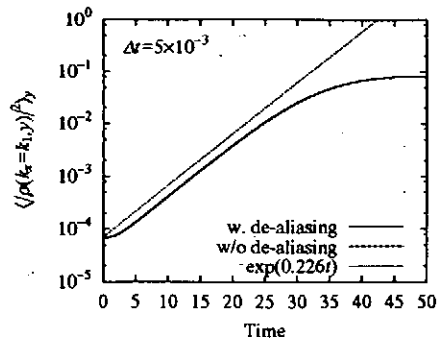

FIG. 6: Time evolutions of the vorticity perturbation amplitude, $\langle |\rho(k_x = k_1, y)|^2 \rangle_y$, in simulations of the Kelvin-Helmholtz instability, where $\langle \cdots \rangle_y$ denotes the spatial average in the y-direction. Simulation results in cases with and without the 2/3-rule for de-aliasing are simultaneously plotted, although they are completely matching to each other. Curves in the linear growth phase are fitted by $\propto \exp(0.226t)$.

Spatial profiles of ρ at $t = 0$, 10, 20, 30, 35, and 50 for the case with de-aliasing are shown in Fig.8 in terms of contour maps. As the K-H instability grows, two vortex islands initially given as the perturbation are stretched in the sheared flow. Accordingly, the vortex sheets are rolling up in the early nonlinear stage of the instability ($t \sim 20$ to 35). Then, a 'noise' with the short wave length becomes dominant in profiles of ρ due to lack of the spatial resolution, as expected from the time evolutions of E and Ω in the case without de-aliasing. It is a natural consequence in numerically solving Eq.(20) with finite resolution, because the finest scale length of ρ in the inviscid fluid could be continuously smaller as the time advances. It is a remedy for this problem to increase the grid number and to stop the simulation before the noise appearance. If we have finer resolution, the noise appears in later time. Even though introduction of the numerical and/or physical dissipation makes the profile of ρ smooth while degrading the enstrophy conservation, it does not accord with the present purpose of benchmarking the nondissipative time-integration scheme.

C. Plasma echo in the drift kinetic system

In order to verify the capability of the nondissipative scheme in Eq.(16) for the phase mixing process, let us consider a plasma echo [30] in a drift kinetic system. The simulation model is the same as that used for the slab ITG turbulent transport [17, 26, 27], and is briefly explained below.

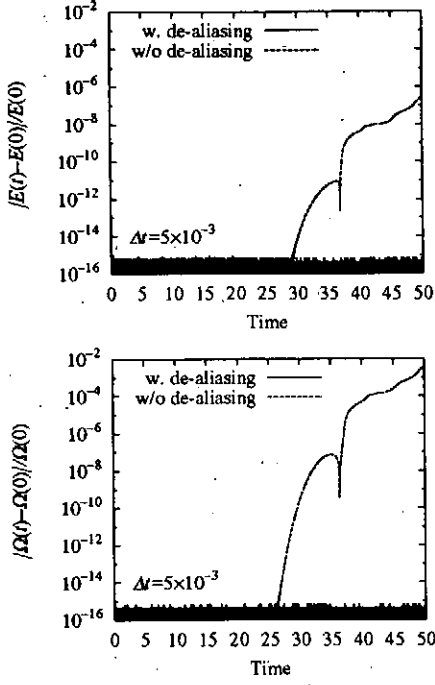The drift kinetic equation for the perturbed ion distri-

FIG. 7: Time evolutions of errors found in conservation of the total energy (top) and the enstrophy (bottom) during the Kelvin-Helmholtz instability obtained by simulations with and without the de-aliasing technique. In the former case, errors are less than 10^{-15}.

bution function $\tilde{f}_k$ with a wave number k is given as

$$\partial_t \tilde{f}_k + i\Theta v_\| k_y \tilde{f}_k + \sum_{k=k'+k''} \left(k'_y k''_x - k'_x k''_y \right) \Psi_{k'} \tilde{f}_{k''}$$
$$= -ik_y \Psi_k \left[1 + \frac{\eta_i}{2} \left\{ v_\|^2 - 1 - k^2 \right\} + \Theta v_\| \right] F_M(v_\|) \quad (23)$$

in a two-dimensional slab geometry with the uniform magnetic field in the y-z plane. Here, the periodic boundary condition is employed both for the x- and y- directions. The gyro-averaged potential ψ_k is related to ϕ_k by

$$\Psi_k = e^{-k^2/2} \phi_k . \quad (24)$$

We set $\Theta = \theta L_n/\rho_i = 1$ where $\theta = B_y/B_z \ll 1$ and ρ_i is the thermal ion gyroradius. The set of equations is closed by the quasi-neutrality condition,

$$\left[1 - \Gamma_0(k^2) \right] \phi_k = e^{-k^2/2} \int \tilde{f}_k(v_\|) dv_\| - \tilde{n}_{e,k} , \quad (25)$$

with the adiabatic electron response,

$$\tilde{n}_{e,k} = \begin{cases} \phi_k & \text{for } k_y \neq 0 \\ 0 & \text{for } k_y = 0 \end{cases} , \quad (26)$$
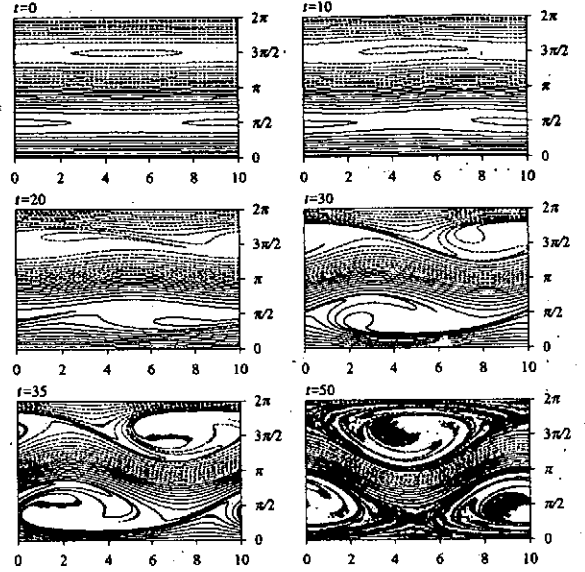
FIG. 8: Contour plots of the vorticity ρ in the Kelvin-Helmholtz instability at $t = 0, 10, 20, 30, 35$, and 50 obtained by the simulation with de-aliasing. Solid and dashed contour lines represent positive and negative values of ρ with the interval of 0.1. The x- and y-axes are in the horizontal and vertical directions, respectively.

where $k^2 = k_x^2 + k_y^2$ and $\Gamma_0(k^2) = \exp(-k^2)I_0(k^2)$. $I_0(z)$ denotes the zeroth order modified Bessel function of z. Equations (23)-(25) are obtained by integrating the gyrokinetic equation [31] for $v_\perp$, assuming $\tilde{f}_k(v_\|, v_\perp) = \tilde{f}_k(v_\|)F_M(v_\perp)$. The above set of equation is normalized as follows; $x = x'/\rho_i$, $y = y'/\rho_i$, $v = v'/v_t$, $t = t'v_t/L_n$, $\eta_i = L_n/L_T$, and $\phi = e\phi'L_n/T_i\rho_i$ with the elementary charge e and the background ion temperature T_i ($= m_i v_t^2$; m_i means the ion mass). We have also taken $T_i = T_e$. The parameter η_i is defined by the ratio between scale lengths of background ion density and temperature gradients, L_n and L_t, although we put $\eta_i = 0$ in simulations of the plasma echo.

The initial perturbed distribution function is set to zero. We also assume the symmetry of $f_{k_x,k_y} = f_{-k_x,k_y}$. Electrostatic potential of $\Phi \cos k_1 x \cos k_1 y$ is externally added at $t = 0$ with a duration time τ_D. The second pulse is given at $t = \tau$ with the wave form of $\Phi \cos k_2 x \cos k_2 y$ for the same period. It is expected that an echo appears through the $E \times B$ nonlinearity, while the parallel nonlinear term is neglected in Eq.(23) due to the gyrokinetic ordering. The appearance time of the echo is estimated as $t = t_{echo} = \tau k_2/(k_2 - k_1)$ [30] with the wave number of $k_{3,x} = k_1 + k_2$ and $k_{3,y} = k_2 - k_1$ [note that the ion diamagnetic drift is in the $(-y)$-direction]. Here, we set $\tau = 30L_n/v_t$, $k_1\rho_i = 0.4$, $k_2\rho_i = 0.5$, $\Phi = 0.1$ and $\tau_D = 0.2L_n/v_t$. Thus, $t_{echo} = 150L_n/v_t$, $k_{3,x}\rho_i = 0.9$, and $k_{3,y}\rho_i = 0.1$.

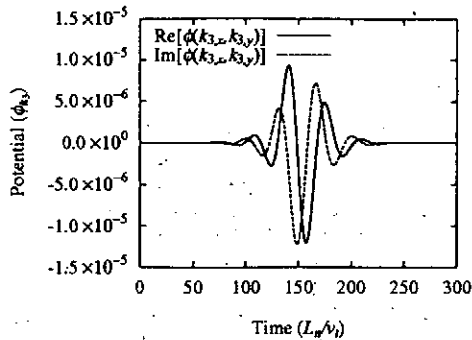The minimum and maximum wave numbers are, re-

FIG. 9: Drift wave echo found in time evolution of the $(k_{3,x}, k_{3,y}) = (k_1 + k_2, k_2 - k_1)$ mode of which potential amplitude peaks at $t = 150 L_n/v_t$ in agreement with the theoretical estimate.

spectively, $0.1\rho_i^{-1}$ and $1.0\rho_i^{-1}$. For de-aliasing in calculation of the $E \times B$ term, the wave number space is extended to $1.5\rho_i^{-1}$, according to the so-called 3/2-rule [29]. The velocity space of $-5v_t \le v_\parallel \le 5v_t$ is represented by 2049 grid points. Since the recurrence time is given by $t_r \equiv 2\pi/k\Delta v_\parallel = 2048\pi/5 \approx 1286 L_n/v_t$, we have enough resolution for the velocity space during the simulation run up to $t = 300 L_n/v_t$. The time step size is set to be $\Delta t = 0.1 L_n/v_t$.

Time evolution of the potential with the wave number of $(k_x, k_y) = (k_1 + k_2, k_2 - k_1)$ is shown in Fig.9. The appearance time of the echo t_{echo} and its wave number $(k_{3,x}, k_{3,y})$ agree with the theoretical estimate. The obtained result demonstrates that the phase mixing process with the time-reversibility is successfully reproduced by the simulation with the nondissipative time-integration scheme.

IV. SUMMARY

This paper has presented a series of benchmark results of the higher-order splitting scheme for the Vlasov-Poisson equations and the nondissipative time-integration method for the collisionless drift kinetic system.

In order to generalize the standard splitting scheme by Cheng and Knorr [2], the explicit symplectic integrators for the separable Hamiltonian system are applied to the mapping of the one-body velocity distribution function. In a test problem for the linear Landau damping, the damping rate obtained by the numerical simulations weakly depends on the order of the time-integrator. Even though an error found in the damping rate is only 3% in the first-order method with a large time step size of $\Delta t \omega_p^{-1} = 1/2$, it is certainly decreased

by using the higher-order methods, where ω_p denotes the angular plasma frequency. In simulations of the nonlinear Landau damping, the invariants (at least, from L^1 to L^5 norms) as well as the entropy $-\int f \ln f dx dv$ are conserved with errors less than 10^{-11} if sufficient resolution holds during the simulation run. By applying the Nth-order splitting scheme, the energy conservation is improved in proportional to Δt^N.

In order to avoid the rapid increase of the entropy and other invariants due to insufficient resolution, a considerable number of grid points are required in the simulations of the nonlinear Landau damping where the Fourier mode interpolation is employed for calculation of the mapping of f. If one would introduce numerical dissipation to suppress the grid-scale fluctuations while preserving the improved energy conservation, a high-order (i.e., Nth-order) interpolation method may be useful, and remains to be investigated. Even if the energy conservation is well satisfied by means of the high-order interpolation scheme, however, introduction of the numerical dissipation will degrade the conservation of the entropy as well as the L^2 norm and higher because of their sensitive dependence on fine-scale structures of the distribution function.

A nondissipative drift kinetic simulation method based on the implicit symplectic integrator is also benchmarked for the Kelvin-Helmholtz (K-H) instability. Conservation of the L^2 norm is an advantage of the nondissipative time-integration scheme. Thus, the energy $E = \int |\nabla \psi|^2 dx dy$ and the enstrophy $\Omega = \int \rho^2 dx dy$ are exactly conserved (except for round-off errors) by employing the nondissipative time-integrator with the de-aliasing technique. Errors found in conservation of E and Ω are as small as the round-off error level of double precision numbers, $\sim O(10^{-15})$. Fine-scale structures of the vorticity are, however, continuously generated because of the nonlinear advection term, which makes the long-time simulation of the K-H instability in an inviscid fluid quite difficult. The test simulation for the plasma echo in the drift kinetic system with a slab geometry demonstrates successful reproduction of the phase mixing process with the time-reversibility. In the present study, the Eulerian approach is employed instead of directly calculating the mapping in Eq.(12) or (13) generated by the implicit symplectic integrator. Since a simulation scheme dealing with the direct calculation of Eq.(12) or (13) may be helpful to realize better conservation of other invariants, further investigations are valuable.

[1] Birdsall, C.K.; Langdon, A.B. *Plasma Physics via Computer Simulation*; McGraw-Hill:New York, 1985.

[2] Cheng, C.Z.; Knorr, G. The Integration of the Vlasov Equation in Configuration Space. J. Comput. Phys. **1976**, 22, 330.

[3] Shoucri, M.; Gagné, R. A Multistep Technique for the Numerical Solution of a Two-Dimensional Vlasov Equation. J. Comput. Phys. bf 1978, 27, 315.

[4] Ghizzo, A.; Izrar, B.; Bertrand, P.; Fijalkow, E.; Feix, M.R.; Shoucri, M. Stability of Bernstein-Green-Kruskal Plasma Equilibria. Numerical Experiments over a Long Time. Phys. Fluids **1988**, 31(1), 72.

[5] Izar, B.; Ghizzo, A.; Bertrand, P.; Fijalkow, E.; Feix, M.R. Integration of Vlasov Equation by a Fast Fourier Eulerian Code. Comput. Phys. Comm. **1989**, 52, 375.

[6] Klimas, A.J.; Farrell, W.M. A Splitting Algorithm for Vlasov Simulation with Filamentation Filtration. J. Comput. Phys. **1994**, 110, 150.

[7] Fijalkow, E. A Numerical Solution to the Vlasov Equation. Comput. Phys. Comm. **1999**, 116, 319.

[8] Nakamura, T.; Yabe, T. Cubic interpolated Propagation Scheme for Solving the Hyper-Dimensional Vlasov-Poisson Equation in Phase Space. Comput. Phys. Comm. **1999**, 120, 122.

[9] Filbet, F.; Sonnendrücker, E.; Bertrand, P. Conservative Numerical Schemes for the Vlasov Equation. J. Comput. Phys. **2001**, 172, 166.

[10] Mangeney, A.; Califano, F.; Cavazzoni, C.; Travnicek, P. A Numerical Scheme for the Integration of the Vlasov-Maxwell System of Equations. J. Comput. Phys. **2002**, 179, 495.

[11] Arber, T.D.; Vann, R.G.L. A Critical Comparison of Eulerian-Grid-Based Vlasov Solvers. J. Comput. Phys. **2002**, 180, 339.

[12] Filbet, F.; Sonnendrücker, E. Comparison of Eulerian Vlasov Solvers. Comput. Phys. Comm. **2003**, 150, 247.

[13] Besse, N.; Sonnendrücker, E. Semi-Lagrangian Schemes for the Vlasov Equation on an Unstructured Mesh of Phase Space. J. Comput. Phys. **2003**, 191, 341.

[14] Forest, E.; Ruth, R.D. Fourth-Order Symplectic Integration. Physica D **1990**, 43, 105.

[15] Yoshida, H. Construction of Higher Order Symplectic Integrators. Phys. Lett. **1990**, 150, 162.

[16] Blanes, S.; Moan, P. Splitting Methods for Non-Autonomous Hamiltonian Equations. J. Comput. Phys. **2001**, 170, 205.

[17] Watanabe, T.-H.; Sugama, H.; Sato, T. A Nondissipative Simulation Method for the Drift Kinetic Equation. J. Phys. Soc. Jpn **2001**, 70(12), 3565.

[18] Ghizzo, A.; Bertrand, P.; Shoucri, M.; Fijalkow, E.; Feix, M.R. An Eulerian Code for the Study of the Drift-Kinetic Vlasov Equation. J. Comput. Phys. **1993**, 108, 105.

[19] Manfredi, G.; Shoucri, M.; Feix, M.R.; Bertrand, P.; Fijalkow, E.; Ghizzo, A. The Numerical Integration of the Vlasov Equation Possessing an Invariant. J. Comput. Phys. **1995**, 121, 298.

[20] Manfredi, G.; Shoucri, M.; Dendy, R.O.; Ghizzo, A.; Bertrand, P. Vlasov Gyrokinetic Simulations of Ion-Temperature-Gradient Driven Instabilities. Phys. Plasmas **1996**, 3(1), 202.

[21] Staniforth, A.; Côté, J. Semi-Lagrangian Integration Schemes for Atmospheric Models – A Review. Mon. Weather Rev. **1991**, 119, 2206.

[22] Sonnendrücker, E.; Roche, J.; Bertrand, P.; Ghizzo, A. The Semi-Lagrangian Method for the Numerical Resolution of the Vlasov Equation. J. Comput. Phys. **1999**, 149, 201.

[23] Shoucri, M. Numerical Simulation of Plasma Edge Turbulence due to E×B Flow Velocity Shear. Czech. J. Phys. **2001**, 51, 1139.

[24] deFrutos, J.; Sanz-Serna, J.M. An Easily Implementable Fourth-Order Method for the Time Integration of Wave Problems. J. Comput. Phys. **1992**, 103, 160.

[25] Sanz-Serna, J.M. Symplectic Runge-Kutta and Related Methods: Recent Results. Physica D **1992**, 60, 293.

[26] Watanabe, T.-H.; Sugama, H.; Sato, T. Nondissipative Kinetic Simulation and Analytical Solution of Three-Mode Equations of the Ion Temperature Gradient Instability. Phys. Plasmas **2000**, 7(3), 984.

[27] Watanabe, T.-H.; Sugama, H. Kinetic Simulation of a Quasisteady State in Collisionless Ion Temperature Gradient Driven Turbulence. Phys. Plasmas **2002**, 9, 3659.

[28] Shoucri, M.; Knorr, G. Linear Instabilities in the Quasistatic Guiding-Center Plasmas. Plasma Phys. **1976**, 18, 187.

[29] Canuto, C.; Hussaini, M.Y.; Quarteroni, A.; Zang, T.A. *Spectral Methods in Fluid Dynamics*; Springer-Verlag, New York, 1988.

[30] Lifshitz, E.M.; Pitaevskii, L.P. *Physical Kinetics*; Pergamon Press, New York, 1981.

[31] Dubin, D.H.E.; Krommes, J.A.; Oberman, C.; Lee, W.W. Nonlinear Gyrokinetic Equations. Phys. Fluids **1983**, 26(12), 3524.

Recent Issues of NIFS Series